ACS APPLIED MATERIALS & INTERFACES

Research Article

www.acsami.org

Charge versus Energy Transfer Effects in High-Performance Perylene Diimide Photovoltaic Blend Films

Ranbir Singh,[†] Ravichandran Shivanna,[‡] Agathaggelos Iosifidis,[§] Hans-Jürgen Butt,[∥] George Floudas,[§] K. S. Narayan,*[,‡] and Panagiotis E. Keivanidis*[,⊥]

[†]Centre for Nanoscience and Technology@PoliMi, Fondazione Istituto Italiano di Tecnologia, Via Giovanni Pascoli 70/3, 20133 Milano, Italy

[‡]Chemistry and Physics of Materials Unit, Jawaharlal Nehru Centre for Advanced Scientific Research, Bangalore 560064, India

[§]Department of Physics, University of Ioannina, 451 10 Ioannina, Greece

[∥]Max Planck Institute for Polymer Research, Ackermannweg 10, D-55128 Mainz, Germany

[⊥]Department of Mechanical Engineering and Materials Science and Engineering, Cyprus University of Technology, Dorothea Bldg, fifth floor, 45 Kitiou Kyprianou Str., Limassol 3041, Cyprus

Supporting Information

ABSTRACT: Perylene diimide (PDI)-based organic photovoltaic devices can potentially deliver high power conversion efficiency values provided the photon energy absorbed is utilized efficiently in charge transfer (CT) reactions instead of being consumed in nonradiative energy transfer (ET) steps. Hitherto, it remains unclear whether ET or CT primarily drives the photoluminescence (PL) quenching of the PDI excimer state in PDI-based blend films. Here, we affirm the key role of the thermally assisted PDI excimer diffusion and subsequent CT reaction in the process of PDI excimer PL deactivation. For our study we perform PL quenching experiments in the model PDI-based composite made of poly[4,8-bis(5-(2-ethylhexyl)thiophen-2-yl)benzo[1,2-*b*;4,5-*b*′]dithiophene-2,6-diyl-*alt*-(4-(2-ethylhexanoyl)-thieno[3,4-*b*]thiophene)-2−6-diyl] (PBDTTT-CT) polymeric donor mixed with the *N*,*N*′-bis(1-ethylpropyl)-perylene-3,4,9,10-tetracarboxylic diimide (PDI) acceptor. Despite the strong spectral overlap between the PDI excimer PL emission and UV−vis absorption of PBDTTT-CT, two main observations indicate that no significant ET component operates in the overall PL quenching: the PL intensity of the PDI excimer (i) increases with decreasing temperature and (ii) remains unaffected even in the presence of 10 wt % content of the PBDTTT-CT quencher. Temperature-dependent wide-angle X-ray scattering experiments further indicate that nonradiative resonance ET is highly improbable due to the large size of PDI domains. The dominance of the CT over the ET process is verified by the high performance of devices with an optimum composition of 30:70 PBDTTT-CT:PDI. By adding 0.4 vol % of 1,8-diiodooctane we verify the plasticization of the polymer side chains that balances the charge transport properties of the PBDTTT-CT:PDI composite and results in additional improvement in the device efficiency. The temperature-dependent spectral width of the PDI excimer PL band suggests the presence of energetic disorder in the PDI excimer excited state manifold.

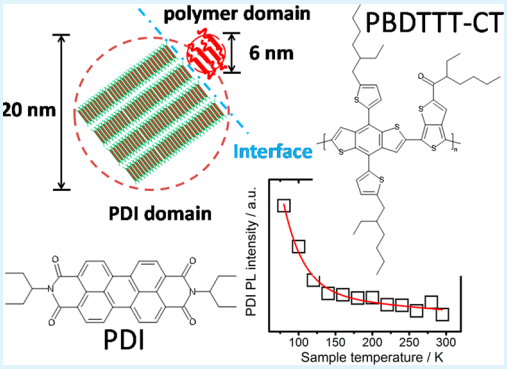

KEYWORDS: *energy transfer, charge transfer, perylene diimide, nonfullerene acceptors, fullerene-free OPVs, excimer dissociation, self-assembly*

INTRODUCTION

Composite films of conjugated polymers mixed with small molecules have been widely studied during the last two decades due to their applicability in organic photovoltaic (OPV) devices.[1−3] Blends of electron-donating polymers and molecular electron acceptors are better known as bulk heterojunctions. They serve as photoactive layers in OPV devices. In a bulk heterojunction the process of charge separation begins after the photoinduced charge transfer at the electron donor/electron acceptor interface. To this date, the most commonly used electron acceptor species are fullerene derivatives due to their excellent electron-accepting strength and charge transport properties.[4,5]

Fullerene derivatives absorb weakly in the visible, and their contribution to the overall photocurrent generation of an OPV device is minimal. In this regard, other electron-accepting molecules can be useful for OPV applications.[6−10] One class of emerging electron-acceptor materials is the family of low-cost perylene dimide derivatives (PDIs).[11−15] PDIs hold great

Received: September 2, 2015
Accepted: October 20, 2015
Published: October 20, 2015

DOI: 10.1021/acsami.5b08224
ACS Appl. Mater. Interfaces 2015, 7, 24876−24886

promise as n-type components in OPV bulk heterojunctions since they exhibit strong absorption in the visible while retaining high thermal, chemical, and photostability properties.[16] Due to their tendency for $\pi-\pi$ interactions, PDIs are known to form self-organized aggregates,[17] a property that in principle can support long-range electron transport.[18−21] PDI organization in OPV blends adapts the structural motif of H-type columnar aggregates,[22] although cases of J-aggregate formation[23] or slip-stacked packing[24] are also possible. In comparison to the fullerene-based OPV devices, the limited mobility of photogenerated charges in PDI-based photoactive layers results in increased nongeminate recombination losses of charges that limit device performance.[25] Recent studies tried to estimate the loss channels in the process of charge photogeneration in an OPV composite of a monomeric PDI derivative and the low energy gap of poly[(4,8-bis(2-ethylhexyloxy)-benzo(1,2-*b*:4,5-*b*′)dithiophene)-2,6-diyl-*alt*-(4-(2-ethylhexanoyl)-thieno[3,4-*b*]thiophene)-2−6-diyl].[26] In PDI blends, light absorption by both components contributes efficiently in polaron generation, and the polaron yield is comparable to that of fullerene blends.[27] Nonetheless, due to inefficient electronic coupling of the PDI domains, electron transport is low, and nongeminate charge recombination losses are high.[21,28] Therefore, more attention is required for improving the overall performance of next generation PDI-based OPV systems.

In a photoexcited PDI columnar mesostructure, excitons convert rapidly (i.e., in the picosecond time scale) to intermolecular states, leading to the generation of excimer states that may act as traps of the absorbed photon energy.[29−31] Excimer states can diffuse albeit in slower than excitons.[32] Consequently, excimer diffusion toward the PDI/polymer interface leads to charge transfer quenching of PDI excimers and charge photogeneration at the interface.[28,33,34] PDI aggregation may impede the transport of the photogenerated charges due to trapping in PDI crystallites[35] that are not electronically connected. Macroscopic electron transport can be facilitated by the propagation of electrons via the dynamically induced electronic coupling of adjacent PDI columns.[36−38] The electronic connectivity of PDI columns is more efficient in the case of PDI domains formed by short-length PDI columns.[28,33]

Recently, promising results have been presented on remedies that can circumvent the detrimental effects of PDI aggregation. The tendency of PDI for the formation of electronically decoupled columns can be reduced either by using nonplanar PDIs derivatives[39−44] or by reducing the size of the PDI columns in the PDI domains.[28] On the basis of these strategies, power conversion efficiencies (PCEs) in the range of 3.7−7.2% have been reported for PDI-based OPV devices.[33,45−48] The enhancement in PCEs has been aided by several device engineering approaches such as use of solvent additives[49−51] and interface modification with the use of suitable electron-collecting interlayers[28,52,53] and with the appropriate selection of device geometry.[34,54]

In spite of the relatively high PCE values obtained from PDI-based excimeric OPV devices the role of PDI excimers in the process of photocurrent generation remains unclear. Particularly when solvent additives, such as the 1,8-diiodooctane (DIO), were used, a clear picture highlighting the effect of additives on the structural properties of the polymer:PDI OPV blends is missing. For PDI derivatives blended with low energy gap polymeric donors, the large spectral overlap between the photoluminescence (PL) spectrum of the PDI excimer and the absorption spectrum of the polymer sets the condition for resonance energy transfer from the PDI component to the polymer phase (Figure 1a). Up to date, the dominant route on the competition between energy transfer and charge transfer in these polymer:PDI blends remains unidentified.

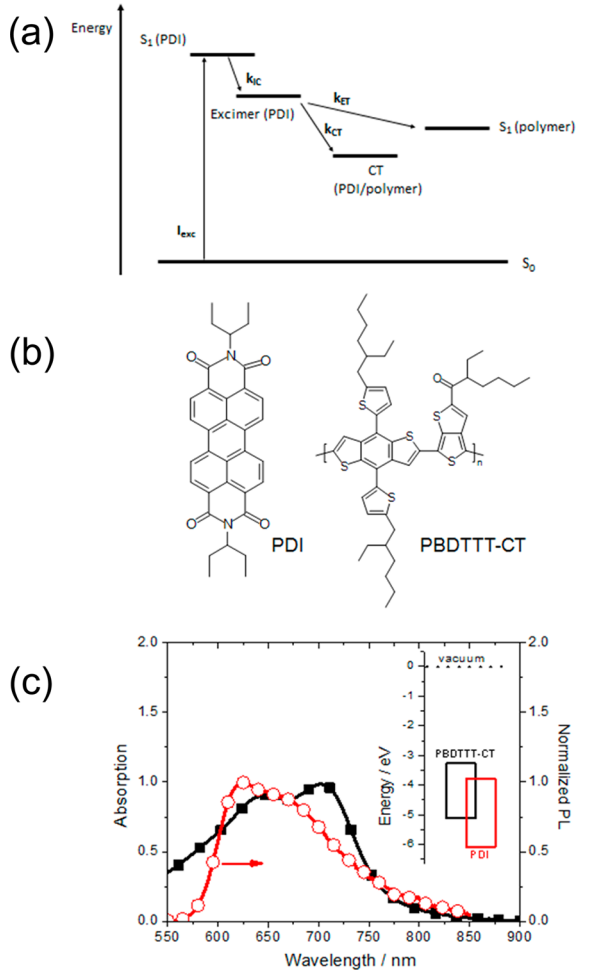

Figure 1. (a) Jablonski diagram depicting the excited state pathway involved in the charge transfer process occurring at the PDI/polymer interface of the PBDTTT-CT:PDI blend. Direct photoexcitation of the PDI component to the S_1 state is followed by a fast internal conversion (k_{IC}) to the PDI excimer state.[29−31] Excimers of PDI can undergo charge transfer (k_{CT}) at the PDI/polymer heterojunction or energy transfer (k_{ET}) to the S_1 state of the polymer component. (b) The chemical structure of the materials used in this study. (c) Spectral overlap between the PBDTTT-CT normalized absorption spectrum (squares) and the PDI excimer normalized PL spectrum (circles). The inset displays the energetics of the PBDTTT-CT:PDI blend system.

According to the Förster theory, resonance energy transfer operates through a nonradiative dipole−dipole coupling mechanism.[55] The energy transfer rate is proportional to the spectral overlap between the PL spectrum of the energy donor and the absorption spectrum of the energy acceptor. In addition, the energy transfer rate is inversely proportional to the sixth power of the separation distance between donor and acceptor species, and for this reason typical energy transfer steps take place for separation distances up to 10 nm.

For fully exploiting the high potential of the low-cost PDI derivatives in OPV applications, a clear understanding is sought on the excited state pathways that govern the flow of the

DOI: 10.1021/acsami.5b08224
ACS Appl. Mater. Interfaces 2015, 7, 24876−24886

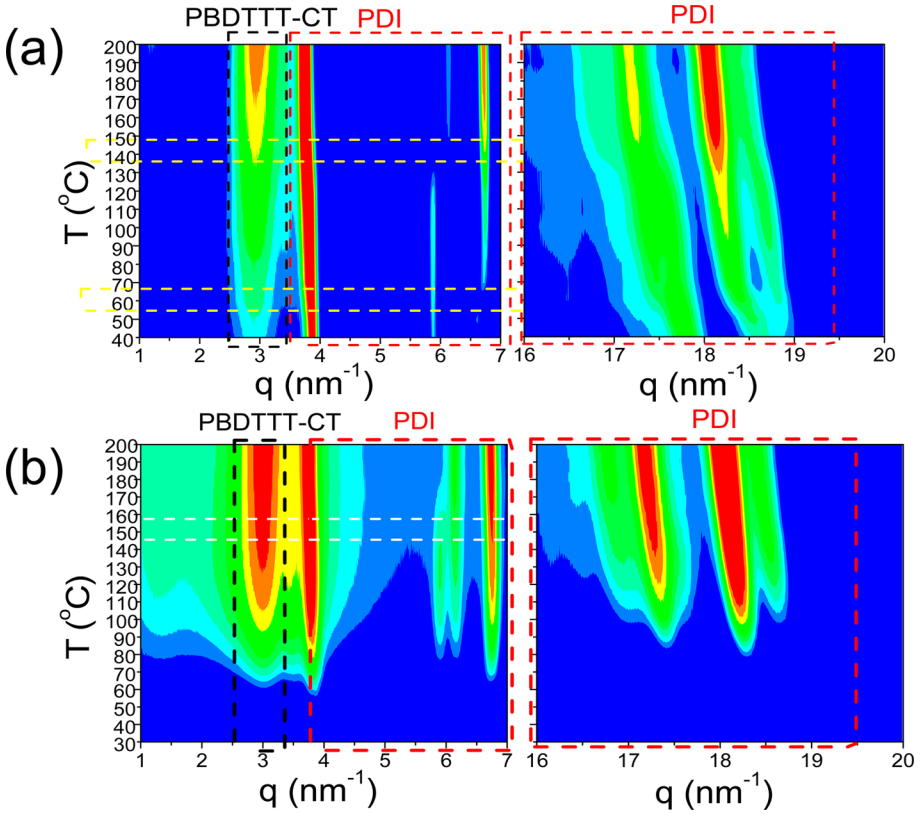

Figure 2. (a) WAXS intensity contour plots as a function of the scattering vector, q, in the lower (left) and higher (right) q regions for the PBDTTT-CT:PDI blend obtained on heating. Diffraction peaks corresponding to backbone-to-backbone correlations (black lines) and to PDI (red lines) are indicated. Horizontal lines (yellow) indicate two phase transitions (see text). Improved backbone-to-backbone correlations as well as improved PDI intracolumnar correlations with increasing temperature are evident from the increasing intensity of the corresponding diffraction peaks. The polymer domain spacing and PDI intracolumnar and intercolumnar characteristic distances at some temperatures are summarized in Table 1. (b) Corresponding intensity contour plots for the PBDTTT-CT:PDI/DIO blend obtained on heating. Lines have the same meaning as in (a).

absorbed photon energy in polymer:PDI OPV blends. Clarifying the routes with which the absorbed photon energy dissipates in the excited state manifolds of the PDI mesostructures will provide valuable feedback to organic chemists for designing the next generation of PDI electron-acceptor adducts and to material scientists for engineering the microstructure of the PDI-based OPV photoactive layers. For this reason we set out to disentangle the processes of energy transfer and charge transfer in the high efficiency PDI-based OPV blend of the *N*,*N*′-bis(1-ethylpropyl)-perylene-3,4,9,10-tetracarboxylic diimide (PDI) monomeric derivative mixed with the poly[4,8-bis(5-(2-ethylhexyl)thiophen-2-yl)benzo[1,2-b;4,5-*b*′]dithiophene-2,6-diyl-*alt*-(4-(2-ethylhexanoyl)-thieno-[3,4-*b*]thiophene)-2−6-diyl] (PBDTTT-CT) polymeric electron donor, by performing temperature-dependent PL spectroscopic characterization. Since both processes manifest in the reduction of the PDI excimer PL intensity, the quantification of the PL quenching alone cannot deconvolute the fraction of the PDI excimers that is quenched by energy transfer to the polymer phase. However, charge transfer of the PDI excimers in the polymer:PDI blends is facilitated via the thermally assisted PDI excimer diffusion toward the PDI/polymer interface. By probing the temperature dependence of PDI excimer PL quenching in the range of 80−295 K we quantify the contribution of the energy and charge transfer processes in the overall PDI excimer PL quenching. Moreover, on the basis of a detailed structural characterization study we elucidate the impact of using the DIO additive on the structural motifs of a polymer:PDI OPV blend. The structural features are discussed with respect to the charge transport properties and the photovoltaic functioning of the corresponding OPV cells.

MATERIALS AND METHODS

Materials. The chemical structures of PBDTTT-CT and PDI materials used in this study are shown in Figure 1. Both the materials were purchased from Solarmer Energy Inc. and used as received.

Solution and Thin-Film Preparation. The solutions of PDI and PBDTTT-CT polymer were prepared by dissolving in chloroform with a concentration of 10 mg/mL. Similarly, a solution of a PBDTTT-CT:PDI (30:70 wt %) mixture was prepared by codissolving PBDTTT-CT with PDI in chloroform with a concentration of 20 mg/mL. All solutions were prepared in a N_2-filled glovebox with overnight stirring. Solutions were spun on the clean glass substrate and were annealed at 100 °C for 15 min in a N_2-filled glovebox.

Time-Integrated UV−vis and PL Spectroscopy. UV−vis absorption and PL spectra of the fabricated films were recorded with a PerkinElmer, Lambda1050 spectrometer and a Horiba Jobin Yvon NanoLog spectrofluorimeter, respectively.

Temperature-Dependent Photoluminescence Measurements. For the PL measurement samples were kept in a custom-made vacuum chamber to avoid degradation of the photoactive layer. The chamber pressure was kept at 10^{-4} m bar to avoid condensation of moisture during the measurement. A 532 nm pulsed laser (Nanolase of ∼10 mW power output) was used to excite the sample at an excitation density of 5 μW/cm^2 using neutral density filters. A fiber-coupled Hamamatsu Minispectrometer (TM-VIS/NIR-C10083CA) was used to acquire the emission spectra from the samples.

2D Wide-Angle X-ray Scattering. Wide-angle X-ray scattering (WAXS) measurements were carried out with a Rigaku MicroMax 007

DOI: 10.1021/acsami.5b08224
ACS Appl. Mater. Interfaces 2015, 7, 24876−24886

rotating anode X-ray generator with a maximum power of 800 W and brightness of 18 kW/mm^2 (operated at a tube voltage of 40 kV and tube current of I = 12 mA (480 W)) utilizing a Cu target. The detection system was a MAR345 image plate area detector, and the sample-to-detector distance was set at 32.5 cm. Extruded fibers (extrusion temperature ∼100 °C) were prepated using a micro-extruder following fast cooling to ambient temperature. Subsequently, the filaments were inserted in a capillary and heated from 30 to 200 °C, in 10 °C steps. At every temperature the diffraction pattern was recorded for 1 h following a 30 min stabilization interval. From the recorded 2-D diffraction patterns the intensity distributions were obtained and presented as a function of the modulus of the scattering vector q [$q = (4\pi/\lambda)\sin(2\theta/2)$, where 2θ is the scattering angle]. Domain sizes were determined from the peak full-width at half-maximum (fwhm).

Solar Cell Fabrication and Characterization. The solar cell device is fabricated on commercially available ITO substrates (sheet resistance ∼10 Ω/square). The ITO substrate was ultrasonically cleaned using acetone and isopropanol for 15 min. After preliminary cleaning, the substrate was cleaned with Hellmanex III to remove contaminants and residues from the ITO surface. The substrate was again cleaned with DI water followed by acetone and isopropanol for 15 min and soon after placed in oxygen plasma (100 W power) for 10 min. Then a film of zinc oxide (ZnO) was spin-coated over the ITO substrate. The glass/ITO/ZnO films were dried in air at 140 °C for 30 min. The sample was then transferred in a N_2-filled glovebox for photoactive layer spin-coating and metal deposition. The solution of PBDTTT-CT:PDI (3:7 wt %) blend was prepared with $CHCl_3$ solvent in a glovebox, and the photoactive film was spin coated on top of a ZnO layer and postannealed at 100 °C for 15 min. Metal electrode V_2O_5/Ag was deposited by thermal evaporation in vacuum (1×10^{-6} m bar) onto the top of a photoactive film. Finally, the device was encapsulated with degassed epoxy and glass slide of 1 mm thickness in the glovebox. The final structure of the OPV device was glass/ITO (140 nm)/ZnO (30 nm)/PBDTTT-CT:PDI (90−106 nm)/V_2O_5 (2 nm)/Ag (90 nm)/encapsulated glass. Identical devices were prepared by inserting 0.4 vol % of the DIO additive in the 30:70 PBDTTT-CT:PDI composite.[33] For all layers fabricated the film thickness was determined by using a Dektak profilometer. The photovoltaic performance of the fabricated solar cells was studied by electrical characterization of the device under simulated solar light (AM1.5G, 98 mW cm^{-2} irradiance), and external quantum efficiency (EQE) was determined with monochromatic illumination.

RESULTS AND DISCUSSION

Figure 1b presents the chemical structures of the electron-accepting monomeric PDI adduct and of the low energy gap electron-donor PBDTTT-CT used in this study. The spectral signature of the PDI excimer in the studied samples exhibits a broad photoluminescence (PL) band between 560 and 850 nm that peaks at 620−630 nm.[13] Due to the spectral overlap between the PL spectrum of the PDI excimer and the absorption spectrum of PBDTTT-CT (see Figure 1c), nonradiative transfer of the PDI excimer energy to the ground-state PBDTTT-CT cannot be excluded. At the same time, the energetics of the PBDTTT-CT:PDI pair (see inset in Figure 1c) favor the charge transfer at the polymer/PDI interface.[33]

2D Wide-Angle X-ray Scattering Characterization. Wide-angle X-ray scattering from extruded fibers of the PBDTTT-CT:PDI 30:70 composite was performed in a range of annealing temperatures on heating and subsequent cooling. Figure 2 presents the contour plots of the WAXS intensity as a function of the scattering wavevector (q) for the blend without and with a DIO additive. The contour plots reveal an intense reflection at lower q associated with the (100) reflection of stacked polymer backbones and several additional reflections at higher q associated with PDI. As a general finding, all reflections become more intense on heating, suggesting improved backbone-to-backbone and PDI correlations. On subsequent cooling from T = 200 °C, the structural order is preserved. By following the respective polymer and PDI reflections as a function of temperature two phase transitions are evident: one at ∼60 °C[13] originating from a change in PDI unit cell and one at ∼140 °C reflecting both polymer and PDI structural changes. In addition to the phase transition temperature, WAXS provides information on the structural order in the blends. In the 30:70 PBDTTT-CT:PDI composite at 100 °C, the PDI and the PBDTTT-CT domain sizes (Ξ_{PDI}, $L_{polymer}$, obtained from the peak fwhm) are ∼23 and ∼4 nm, respectively. The PDI domains increase further on heating (to Ξ_{PDI} ∼ 30 nm at 200 °C) suggesting increasing phase separation by annealing at higher temperatures. The PDI domains are comprised of PDI molecules that self-organize into columnar stacks of ∼17 nm length (about 50 disks per column). The temperature-dependent domain sizes of the blend components are reported in the Supporting Information (see Table S1).

Interestingly, the addition of a small amount, i.e., 0.4 vol %, of the DIO additive[33] influences both the polymer backbone and PDI domains. The PBDTTT-CT characteristic backbone-to-backbone distance is reduced by roughly 3% (from 2.17 to 2.10 nm at T = 100 °C). Furthermore, the polymer characteristic domain (L) is enlarged from 4 to 6 nm at T = 100 °C. These both suggest a softening of interactions for the polymer backbone by DIO that acts as a plasticizer. A similar effect of DIO was described in films of small molecule:fullerene OPV composites.[56] In this respect, the alkyl chains of DIO mix with the branched ethyl chains of the polymer and better facilitate polymer packing. Concerning the packing of the PDI component, DIO does not alter the intercolumnar and intracolumnar distances (d_{inter} = 1.68 nm and d_{intra} = 0.34 nm, at T = 200 °C, respectively). However, unlike with the polymer domain, the size of PDI domains is reduced from Ξ_{PDI} ∼ 30 nm to ∼22 nm at 200 °C. Given the high boiling point of the DIO component (ca. 168 °C) it is expected that some DIO content is remaining in the OPV layer following solvent evaporation.The WAXS findings suggest that the remaining DIO is located in part within the polymer domains, where by plasticization it improves the backbone-to-backbone correlations, and in part at the interface with the PDI domains.

Time-Integrated Photoluminescence Characterization at Low Temperatures. Steady-state PL measurements after selective photoexcitation of the PDI component monitored the PL quenching of the PDI excimer emission in the PBDTTT-CT:PDI blends. At room temperature and in comparison to the PDI-only film, the PDI excimer PL emission intensity of the PBDTTT-CT:PDI blend films was reduced. For estimating the magnitude of the PL quenching, control films of PS:PDI were fabricated having the same PDI content as the PBDTTT-CT:PDI films. The relative comparison of the PDI excimer PL signal found that the PL quenching efficiency (Φ_q) of PBDTTT-CT:PDI blends increases as the PDI content in the blend decreases (see Figure S1 in Supporting Information). Table 1 reports the composition-dependent Φ_q values of the PL quenching experiment at room temperature. The possible origins of the observed PL quenching in the PBDTTT-CT:PDI blends can originate from (i) an energy transfer from photoexcited PDI to the ground state of PBDTTT-CT or

DOI: 10.1021/acsami.5b08224
ACS Appl. Mater. Interfaces 2015, 7, 24876−24886

Table 1. PL Quenching Efficiency (Φ_q) at 295 K for the PBDTTT-CT:PDI (10:90), PBDTTT-CT:PDI (30:70), and PBDTTT-CT:PDI (50:50) Blends with Respect to the Reference PS:PSI Film of the Same Composition As Shown in Supporting Information Figure S4[a]

system	Φ_q (%) at 295 K	$E_{a,190K-295K}$ (meV)	$E_{a,80K-190K}$ (meV)
PDI-only	–	−26	-
PBDTTT-CT:PDI (10:90)	70	−22	−111
PBDTTT-CT:PDI (30:70)	93	−27	−164
PBDTTT-CT:PDI (50:50)	95	−22	−170

[a]The activation energy, E_a, as extracted by eq 1 for these composites.

(ii) a charge transfer between photoexcited PDI and PBDTTT-CT.

Time-integrated PL spectra of PBDTTT-CT:PDI blends with various PDI content were recorded in a range of temperatures between 80 and 290 K by photoexciting the PDI component at 532 nm. Figure 3 gives an overview of the temperature-dependent PL study for a PDI-only film together with the results obtained for the three PBDTTT-CT:PDI compositions of 10:90, 30:70, and 50:50 ratios.

The films were initially cooled to 80 K, and PL spectra were recorded on heating at 10 K temperature intervals up to room temperature. All recorded PL spectra were fitted with a Gaussian function in order to obtain the individual peak energy and the fwhm parameters of vibronic transitions (Supporting Information, Figure S2). The rise in temperature results in distinct spectral changes in the PL spectra of all samples measured. More specifically, the PL peak positioning and the maximum PL intensity are clearly affected as temperature rises. Likewise, the increase in temperature also affects the spectral width of the PDI excimer PL signal. As an example, the fwhm value of the PBDTTT-CT:PDI 30:70 blend at 80 K is found at 0.064 eV, whereas at 295 K it reaches 0.110 eV (Supporting Information, Figure S3). Figure 3a presents the temperature-dependent peak PDI excimer energy (E_{peak}) and the respective PL excimer intensity of the pristine PDI film normalized to the maximum PL intensity at 80 K. Similarly, Figure 3b, c, d presents the blue shift observed in the E_{peak} parameter with the rise in temperature, for all three compositions of the PBDTTT-CT:PDI films. Clearly, E_{peak} exhibits a hypsochromic shift with increasing temperature, from 1.95 eV at 80 K to 1.99 eV at 290 K. In all samples, the PDI excimer PL intensity is maximized at 80 K, and it is gradually reduced with increasing temperature, indicating that at low temperatures the PL quenching becomes less efficient.

The temperature-dependent PL data of Figure 3 can be discussed in the context of the Arrhenius formalism. Equation 1 represents an Arrhenius temperature-dependent PL intensity with negative activation energy E_a. The kinetic scheme for deriving eq 1 is provided in the Supporting Information. Here the parameter B corresponds to the pre-exponential factor related to the PDI excimer PL process.

$$\ln I_{PL} = \ln B + \frac{E_a}{R}\frac{1}{T} \quad (1)$$

Figure 4 gives the Arrhenius plots for the PDI-only film and the three PBDTTT-CT:PDI composites of 10:90, 30:70, and 50:50

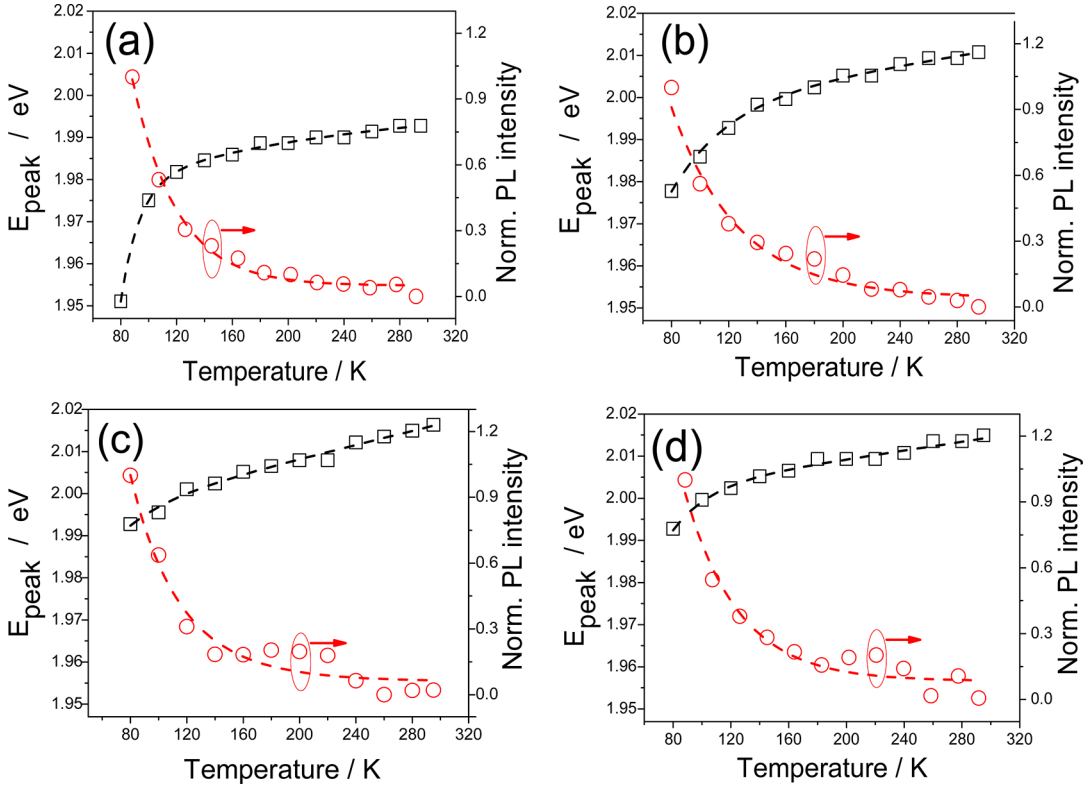

Figure 3. Temperature-dependent PL peak energy (black squares) and normalized PL peak intensity (red circles) of the PL spectra obrained for (a) pristine PDI, (b) PBDTTT-CT:PDI, 10:90, (c) PBDTTT-CT:PDI, 30:70, and (d) PBDTTT-CT:PDI, 50:50 blend films. Dashed lines are a guide for the eye.

DOI: 10.1021/acsami.5b08224
ACS Appl. Mater. Interfaces 2015, 7, 24876−24886

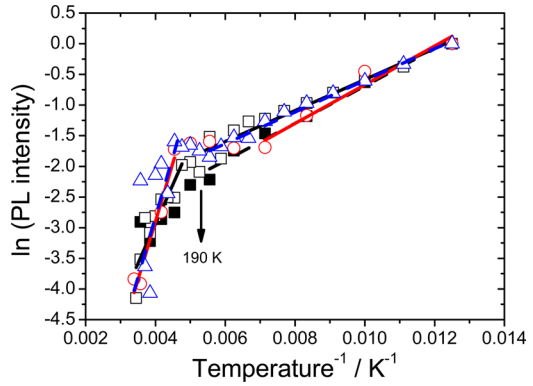

Figure 4. PL intensity of the PDI excimer as a function of the reciprocal of the absolute temperature for layers prepared by PDI-only (filled squares) and by 10:90 (open squares), 30:70 (open circles), and 50:50 (open triangles) PBDTTT-CT:PDI blends. The slope of the relationship is a measure of the activation energy (see eq 1), and two distinct activation energies can be derived for the PBDTTT-CT:PDI systems: the first before and the second after T = 190 K.

composition, whereas the corresponding activation energies E_a extracted from eq 1 are reported in Table 1. Two distinct temperature regimes are identified for the PBDTTT-CT:PDI composites: between 80 and 190 K with $|E_a| \gg k_BT$ and between 200 and 295 K with $|E_a| \sim k_BT$, where k_B corresponds to the Boltzmann constant and T to the absolute temperature. Only in the case of the PDI-only system a single activation energy was deduced across the whole temperature range studied. Table 1 reports the deduced E_a values of all measured systems. The negative sign of the activation energy indicates that the PL of the PDI excimer is barrierless,[57] therefore underlining the barrier-limited character of the PL quenching process. The activation energy for the PL quenching of the PDI excimer becomes significant at temperatures lower than 190 K, obtaining absolute values higher than 100 meV (see Table 1) that increase as the PDI content of the PBDTTT-CT:PDI blend reduces.

The photophysical characterization of the PBDTTT-CT:PDI composites finds that that the process of energy transfer has a negligible effect on the PL quenching of the PDI excimers. By selectively photoexciting the PDI component of the PBDTTT-CT:PDI blends, PDI excimers are rapidly formed, and they dissociate by charge transfer at the PDI/polymer interface. Both temperature-dependent PL and composition-dependent PL characterization experiments verify that PL quenching of the PDI excimers is dominated by a charge transfer process. In particular, the temperature-dependent PL study finds that by decreasing temperature the intensity of the PDI excimer PL band increases significantly. In contrast, a potential quenching of the PDI excimer PL emission via a resonance energy transfer to the PBDTTT-CT phase would be temperature independent.[55] This is direct evidence for the participation of the thermally activated PDI excimer diffusion toward the PDI/polymer interfaces. At low temperatures, both processes of nonradiative relaxation to the ground state and of PDI excimer diffusion are suppressed. The latter is in agreement with the negative activation energy extracted by the Arrhenius plots (see Figure 4 and Table 1).

The composition-dependent PL quenching experiments verify further that energy transfer from the PDI excimer to PBDTTT-CT is negligible. Several studies of the Förster energy transfer mechanism in emitter/quencher solid state mixtures have shown that trace amounts of the quencher are sufficient for fully quenching the PL signal of the emitter.[58] In contrast, we observe that when a PDI-only film is loaded with 10 wt % PBDTTT-CT content (i.e., in the 10:90 PBDTTT-CT:PDI sample) the room-temperature PL quenching efficiency, Φ_q, of the PDI excimer is inefficient, and a much higher PBDTTT-CT loading is required for fully quenching the PDI excimer PL emission (see Table 1). The results highlight the necessity for having a high concentration of PDI/PBDTTT-CT interfaces that will facilitate the charge transfer induced dissociation of the PDI excimers. Finally, on the basis of the structural data provided by WAXS (see Table S1) the energy transfer from the PDI excimer to the PBDTTT-CT polymer seems unlikely. At a molecular level, the PDI aggregates are formed by the coalescence of PDI domains that comprise self-organized PDI columns bundled together. The length of the PDI columns can be tuned by thermal annealing, whereas the size of the PDI domains is less sensitive to thermal treatment maintaining a size of 20−25 nm. This relatively large size of the PDI domains is much larger than the typical donor−acceptor distances of 10 nm that comply with the dipole-based energy transfer mechanism described by the Förster theory. It is worth noting that the fraction of the PDI excimer states that manage to undergo energy transfer toward the PBDTTT-CT phase may undergo charge transfer at the PBDTTT-CT/PDI interface, albeit with some time delay.[26]

For all films investigated herein, the E_{peak} of the PDI excimer PL band blue shifts, and the corresponding fwhm of the PL band increases with increasing temperature (Figure 3a−d), confirming that energetic disorder is present in the density of states of these systems.[59−61] Energetic disorder in polymer:PDI blends is expected when a distribution of molecular packing arrangements exists for the PDI molecules,[34] and this can influence the performance of the PDI-based solar cell devices.[33] At present, the PL data shown in Figure 3 can provide information concerning the spectral signature of energetic disorder by quantifying the magnitude of electron−phonon coupling in the PBDTTT-CT:PDI blends. In principle, electron−phonon interactions reflect the magnitude of the geometrical deformation in the excited state after photoexcitation, which is quantified by the Huang−Rhys parameter S.[62] The latter is experimentally calculated by the PL intensity ratio I_{01}/I_{00} where I_{01} and I_{00} correspond to 0−0 and 0−1 vibronic transitions.[63−66] The spectral intensities of the transitions between the 0th vibrational level in the electronic excited state and the nth vibronic level in the ground state are approximated by

$$I_{0\rightarrow n} = \frac{e^{-S}S^n}{n!} \quad (2)$$

where S is the Huang−Rhys factor. The magnitude of the electron−phonon coupling in each of the composites, as expressed by the Huang−Rhys parameter, indirectly reflects the structural order of the PDI domains for the different PBDTTT-CT:PDI compositions. In this approach the electron−phonon coupling serves as a spectroscopic probe for monitoring the fraction of the PDI domains assessed by the PDI excimer during its lifetime.

At room temperature, the PDI-only film exhibits the highest value of the Huang−Rhys parameter. This is in line with the notion that the PDI domains in the PDI-only system are better ordered than in PBDTTT-CT:PDI blends, as also verified by the WAXS data. Similarly, for the higher-PDI content

DOI: 10.1021/acsami.5b08224
ACS Appl. Mater. Interfaces 2015, 7, 24876−24886

PBDTTT-CT:PDI (10:90 and 30:70) blends, the Huang–Rhys parameter is comparable with $S = 0.32$, but as the PDI content decreases further in the 50:50 PBDTTT-CT:PDI sample, the Huang–Rhys parameter reduces to $S = 0.24$. The dependence of the Huang–Rhys on PDI content becomes clearer at lower temperatures where the electron–phonon coupling in the PDI and PBDTTT-CT:PDI films increases. Figure 5 gives the

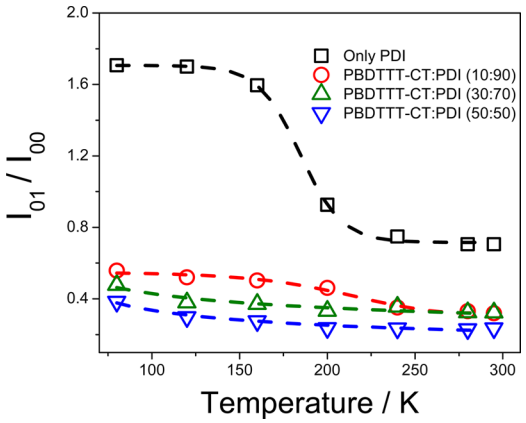

Figure 5. I_{01}/I_{00} PL intensity ratio of the resolved peaks in the PL spectrum of the PDI-only, PBDTTT-CT:PDI (10:90), PBDTTT-CT:PDI (30:70), and PBDTTT-CT:PDI (50:50) film as a function of temperature.

calculated I_{01}/I_{00} PL intensity ratio for the pristine PDI film and for the PBDTTT-CT:PDI blend films across the whole range of low temperatures studied. An increase in the electron–phonon coupling is found as the PDI content of the PBDTTT-CT:PDI composites is increased.

Microscopy Imaging Characterization. Further information on the morphology-related properties of the PDI-only and PBDTTT-CT:PDI composite layers at higher length scales is obtained from confocal microscopy (ZEISS, LSM 700) and atomic force microscopy (JPK Instruments Inc, Nanowizard 3) imaging. A PBDTTT-CT-only film was also characterized for reference purposes (see Figure S4). Figure 6a–d presents confocal microscopy fluorescent images of PDI-only and PBDTTT-CT:PDI blend films with different ratios; PDI-only and 10:90, 30:70, and 50:50 PBDTTT-CT:PDI films. All optical images were obtained by probing the PDI excimer emission centered at around 630 nm,[21] by scanning an area of $25 \times 25\ \mu m^2$ in reflection mode following laser photoexcitation at 532 nm. For all samples ribbon-like features are observed attributed to the formation of PDI aggregates.[21] Table 2 reports the dimensions of the aggregates as a function of PDI content in the blends, as determined by the analysis of the confocal microscope images.

Table 2. Composition-Dependent Average Values of Width and Length of the PDI Aggregates and the Surface Roughness of the Layers Studied in This Work

system	width (μm)	length (μm)	R_{RMS} (nm)	$R_{average}$ (nm)
PDI-only	0.50 ± 0.03	1.25 ± 0.45	9.3	7.3
PBDTTT-CT:PDI (10:90)	0.35 ± 0.10	0.95 ± 0.10	7.5	5.8
PBDTTT-CT:PDI (30:70)	0.30 ± 0.20	1.35 ± 0.40	10.6	8.2
PBDTTT-CT:PDI (50:50)	0.20 ± 0.02	0.60 ± 0.04	13.8	8.6

A gradual reduction in the width of the PDI ribbons is found with decreasing PDI component. For the PDI-only film the width of the ribbons is 0.50 ± 0.03 μm, whereas for the 50:50 PBDTTT-CT:PDI blends it is reduced to 0.20 ± 0.02 μm. Instead, no effect of the thermal annealing temperature is observed on the PDI aggregate length.

Figure 6e–h presents the tapping mode atomic force microscopy (AFM) images of the PDI-only and PBDTTT-CT:PDI blend films that were used for the confocal microscopy imaging experiments. The root-mean-square and average roughness values of the films are summarized in Table 2. The average roughness of the film increases with decreasing PDI content, but the surface of all films remains rougher than the surface of the PBDTTT-CT-only layer of comparable thickness, ca. 80–90 nm ($R_{RMS} = R_{average} = 0.5$ nm, see Figure S4), annealed at 100 °C for 15 min.

Electrical Characterization of Solar Cell Devices. Figure 7 depicts external quantum efficiency (EQE) spectra and the photocurrent density–voltage (J–V) characteristics of OPV devices prepared by photoactive layers of PDI-only and PBDTTT-CT:PDI blends with 10:90, 30:70, and 50:50

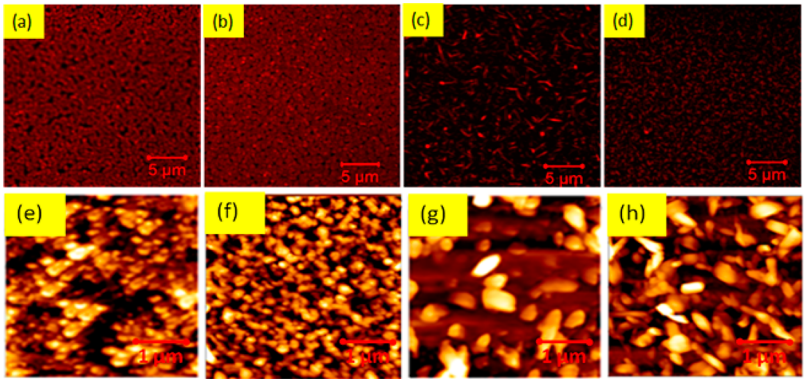

Figure 6. First row: the confocal microscopy images for (a) pristine PDI film, (b) film PBDTTT-CT:PDI (10:90), (c) PBDTTT-CT:PDI (30:70), and (d) PBDTTT-CT:PDI (50:50) blend film. Second row: atomic force microscopy (AFM) images for (e) pristine PDI film, (f) PBDTTT-CT:PDI (10:90), (g) PBDTTT-CT:PDI (30:70), and (h) PBDTTT-CT:PDI (50:50) blend film. In confocal microscopy all films were excited with 532 nm laser, and images were captured in reflection mode with an 100× objective. Films were spun on a glass substrate and thermally annealed at a temperature of 100 °C for 15 min in a nitrogen-filled glovebox.

DOI: 10.1021/acsami.5b08224
ACS Appl. Mater. Interfaces 2015, 7, 24876–24886

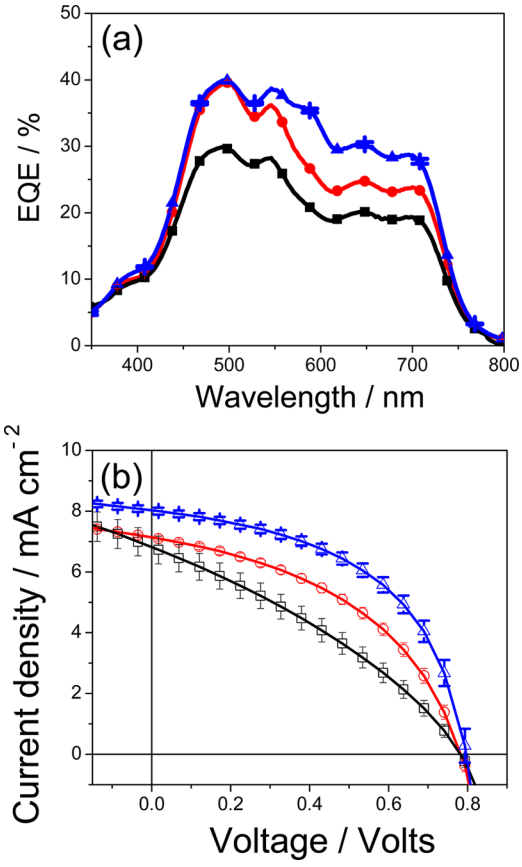

Figure 7. (a) External quantum efficiency (EQE) spectra of PBDTTT-CT:PDI devices with composition of 50:50 (filled squares), 30:70 (filled circles), and 30:70 + 0.4 vol % DIO (filled triangles). (b) $J-V$ characteristic of PBDTTT-CT:PDI devices with composition of 50:50 (open squares), 30:70 (open circles), and 30:70 + 0.4 vol % DIO (open triangles).

polymer:PDI ratios. A nearly vanishing photovoltaic effect was found for the devices with photoactive layers of the PDI-only and the PBDTTT-CT:PDI 10:90 systems. With increasing polymer content in the PBDTTT-CT:PDI composites the Φ_q value for the PDI excimer surpasses 90% (see Table 1), and photocurrent generation becomes more efficient. The EQE spectra of the PBDTTT-CT:PDI with 30:70 and 50:50 content in Figure 7 match with the absorption spectra of the corresponding PBDTTT-CT:PDI blend films (Figure S5) confirming that light absorbed by the PBDTTT-CT and the PDI phases results in the production of photocurrent. The comparison of the EQE values at the spectral ranges where either the PDI component or the PBDTTT-CT component mainly absorb light indicate that both species contribute to the photocurrent generation efficiency in a comparable manner. The corresponding device metrics, namely, the short-circuit current density (J_{sc}), open-circuit voltage (V_{oc}), fill factor (FF), and the PCE parameter are reported in Table 3. The device with PBDTTT-CT:PDI (30:70) blend film shows the best device characteristics: J_{sc} = 7.2 ± 0.13 mA/cm^2, V_{oc} = 0.79 ± 0.006 V, FF = 45 ± 1.1%, PCE = 2.82 ± 0.11%, and EQE$_{max}$ = 40%. The relatively higher PCE value obtained for the 30:70 device is attributed to the proper PBDTTT-CT:PDI ratio that ensures the complete dissociation of the PDI excimer at the PDI/polymer interfaces and to the optimized connectivity of the PDI domains that favor efficient charge photogeneration and balanced charge transport properties. The latter was confirmed by space charge limited current measurements (Supporting Information, Figure S6). By using a small amount of DIO (0.4 vol %) for processing the 30:70 PBDTTT-CT:PDI photoactive layer the charge transport is balanced further, testifying the positive impact of the DIO-induced structural reorganization observed in WAXS. Higher PCE values, in the order of 3.7%, can be obtained when this small amount of the DIO additive is used.[33] The EQE spectrum and the corresponding $J-V$ characteristics of the DIO-containing PBDTTT-CT:PDI device are shown in Figure 7 in comparison with the data of the DIO-free PBDTTT-CT:PDI devices. Table 3 reports the main device figures of merit for this device.

CONCLUSIONS

A temperature-dependent photophysical study was performed for the technologically important PBDTTT-CT:PDI OPV blends in combination with detailed structural and electrical characterization experiments. In binary polymer:PDI blends energetic disorder is caused by the distribution of the packing arrangements of the PDI molecules. Apparently, energy transfer seems to compete with charge transfer in the overall deactivation of the photoinduced PDI excimer state, and the proportional contribution of each of these two photophysical processes remains still unresolved. Our results offer a direct answer to this hitherto troubling puzzle. We clearly demonstrate that the energy transfer of the PDI excimers to the polymer phase has a negligible role on the overall consumption of the PDI excimer energy and that PDI excimers primarily charge transfer at the PDI/polymer interfaces. Despite the strong spectral overlap between the PL spectrum of the PDI excimer and the UV–vis absorption of the PBDTTT-CT polymer, the process of nonradiative energy transfer cannot be held responsible for the observed PL quenching of the PL emission of the PDI excimer. Our suggestion is verified by temperature-dependent PL characterization measurements that find an increased PL signal at lower temperatures and by composition-dependent PL quenching measurements that demonstrate an inefficient PL quenching of the PDI excimer state even when the relative PBDTTT-CT polymer content is as high as 10 wt %. Both experimental observations contradict an energy transfer mechanism. Instead,

Table 3. OPV Device Characteristics for the Photoactive Layers of PDI-only, PBDTTT-CT:PDI (10:90), PBDTTT-CT:PDI (30:70), PBDTTT-CT:PDI (50:50) and PBDTTT-CT:PDI (30:70) + 0.4 vol.% DIO

system	V_{oc} (V)	J_{sc} (mA/cm^2)	FF (%)	PCE (%)	PCE$_{max}$
PDI-only	-	-	-	-	-
PBDTTT-CT:PDI (10:90)	0.08 ± 0.12	3.0 ± 0.42	31.0 ± 1.9	0.18 ± 0.01	0.19
PBDTTT-CT:PDI (30:70)	0.78 ± 0.01	7.2 ± 0.17	44.7 ± 0.9	2.70 ± 0.17	2.87
PBDTTT-CT:PDI (50:50)	0.78 ± 0.01	6.8 ± 0.30	35.4 ± 1.3	1.92 ± 0.12	2.04
PBDTTT-CT:PDI (30:70) + 0.4 vol % DIO	0.80 ± 0.01	8.1 ± 0.06	51.9 ± 0.7	3.60 ± 0.10	3.70

DOI: 10.1021/acsami.5b08224
ACS Appl. Mater. Interfaces 2015, 7, 24876–24886

they suggest a thermally assisted charge-transfer-based PL quenching mechanism of the PDI excimer state.

The morphology of the PBDTTT-CT:PDI blend films changes as the PDI content varies. Concerning device applications, the optimum PBDTTT-CT:PDI component ratio is found to be 30:70. In line with previous reports, further improvement in OPV device performance is achieved when 0.4 vol % of DIO is added. The structural characterization of the PBDTTT-CT:PDI+DIO system reveals the actual role of the DIO component; the ethylene-like structure of DIO "plasticizes" the polymer side chains and balances charge carrier mobility.

This work provides deeper insight toward the development of next generation multiadduct PDI electron acceptors that can be utilized in high-performance fullerene-free photoactive devices such as organic solar cells and organic photodetectors.

■ ASSOCIATED CONTENT

Supporting Information

The Supporting Information is available free of charge on the ACS Publications website at DOI: 10.1021/acsami.5b08224.

Temperature-dependent polymer domain spacing and PDI intracolumnar and intercolumnar characteristic distances of the PBDTTT-CT:PDI blends with and without DIO, composition- and temperature-dependent photoluminescence data of PBDTTT-CT:PDI films, derivation of the kinetic Arrhenius scheme, confocal microscopy and atomic force microscopy images of a thermally annealed PBDTTT-CT film, composition-dependent absorption coefficient spectra of PBDTTT-CT:PDI films, space charge limited current data of PBDTTT-CT:PDI electron-only and hole-only devices (PDF)

■ AUTHOR INFORMATION

Corresponding Authors

*E-mail: narayan@jncasr.ac.in.

*E-mail: p.keivanidis@cut.ac.cy.

Notes

The authors declare no competing financial interest.

■ REFERENCES

(1) Brabec, C. J.; Sariciftci, N. S.; Hummelen, J. C. Plastic Solar Cells. *Adv. Funct. Mater.* **2001**, *11*, 15−26.

(2) Dou, L.; You, J.; Hong, Z.; Xu, Z.; Li, G.; Street, R. A.; Yang, Y. 25th Anniversary Article: A Decade of Organic/Polymeric Photovoltaic Research. *Adv. Mater.* **2013**, *25*, 6642−6671.

(3) He, Z. C.; Zhong, C. M.; Su, S. J.; Xu, M.; Wu, H. B.; Cao, Y. Enhanced Power-Conversion Efficiency in Polymer Solar Cells Using an Inverted Device Structure. *Nat. Photonics* **2012**, *6*, 593−597.

(4) Scharber, M. C.; Muhlbacher, D.; Koppe, M.; Denk, P.; Waldauf, C.; Heeger, A. J.; Brabec, C. L. Design Rules for Donors in Bulk-Heterojunction Solar Cells - Towards 10% Energy-Conversion Efficiency. *Adv. Mater.* **2006**, *18*, 789−794.

(5) Service, R. F. Outlook Brightens for Plastic Solar Cells. *Science* **2011**, *332*, 293−293.

(6) Lin, Y.; Zhan, X. Non-Fullerene Acceptors for Organic Photovoltaics: An Emerging Horizon. *Mater. Horiz.* **2014**, *1*, 470−488.

(7) Li, H.; Earmme, T.; Ren, G.; Saeki, A.; Yoshikawa, S.; Murari, N. M.; Subramaniyan, S.; Crane, M. J.; Seki, S.; Jenekhe, S. A. Beyond Fullerenes: Design of Nonfullerene Acceptors for Efficient Organic Photovoltaics. *J. Am. Chem. Soc.* **2014**, *136*, 14589−14597.

(8) Kwon, O. K.; Park, J.-H.; Park, S. K.; Park, S. Y. Soluble Dicyanodistyrylbenzene-Based Non-Fullerene Electron Acceptors with Optimized Aggregation Behavior for High-Efficiency Organic Solar Cells. *Adv. Energy Mater.* **2015**, *5*, 1400929.

(9) Holliday, S.; Ashraf, R. S.; Nielsen, C. B.; Kirkus, M.; Röhr, J. A.; Tan, C.-H.; Collado-Fregoso, E.; Knall, A.-C.; Durrant, J. R.; Nelson, J.; McCulloch, I. A Rhodanine Flanked Nonfullerene Acceptor for Solution-Processed Organic Photovoltaics. *J. Am. Chem. Soc.* **2015**, *137*, 898−904.

(10) McAfee, S. M.; Topple, J. M.; Hill, I. G.; Welch, G. C. Key Components to the Recent Performance Increases of Solution Processed Non-Fullerene Small Molecule Acceptors. *J. Mater. Chem. A* **2015**, *3*, 16393.

(11) Tang, C. W. Two-Layer Organic Photovoltaic cell. *Appl. Phys. Lett.* **1986**, *48*, 183−185.

(12) Schmidt-Mende, L.; Fechtenkotter, A.; Mullen, K.; Moons, E.; Friend, R. H.; MacKenzie, J. D. Self-organized Discotic Liquid Crystals for High-Efficiency Organic Photovoltaics. *Science* **2001**, *293*, 1119−1122.

(13) Keivanidis, P. E.; Howard, I. A.; Friend, R. H. Intermolecular Interactions of Perylene Diimides in Photovoltaic Blends of Fluorene Copolymers: Disorder Effects on Photophysical Properties, Film Morphology and Device Efficiency. *Adv. Funct. Mater.* **2008**, *18*, 3189−3202.

(14) Kamm, V.; Battagliarin, G.; Howard, I. A.; Pisula, W.; Mavrinskiy, A.; Li, C.; Muellen, K.; Laquai, F. Polythiophene:Perylene Diimide Solar Cells - the Impact of Alkyl-Substitution on the Photovoltaic Performance. *Adv. Energy Mater.* **2011**, *1*, 297−302.

(15) Sharenko, A.; Proctor, C. M.; van der Poll, T. S.; Henson, Z. B.; Nguyen, T.-Q.; Bazan, G. C. A High-Performing Solution-Processed Small Molecule: Perylene Diimide Bulk Heterojunction Solar Cell. *Adv. Mater.* **2013**, *25*, 4403−4406.

(16) Zhan, X.; Facchetti, A.; Barlow, S.; Marks, T. J.; Ratner, M. A.; Wasielewski, M. R.; Marder, S. R. Rylene and Related Diimides for Organic Electronics. *Adv. Mater.* **2011**, *23*, 268−284.

(17) Tasios, N.; Grigoriadis, C.; Hansen, M. R.; Wonneberger, H.; Li, C.; Spiess, H. W.; Müllen, K.; Floudas, G. Self-Assembly, Dynamics, and Phase Transformation Kinetics of Donor-Acceptor Substituted Perylene Derivatives. *J. Am. Chem. Soc.* **2010**, *132*, 7478.

(18) Jancy, B.; Asha, S. K. Hydrogen-Bonding-Induced Conformational Change from J to H Aggregate in Novel Highly Fluorescent Liquid-Crystalline Perylenebisimides. *Chem. Mater.* **2008**, *20*, 169−181.

(19) Singh, T. B.; Erten, S.; Guenes, S.; Zafer, C.; Turkmen, G.; Kuban, B.; Teoman, Y.; Sariciftci, N. S.; Icli, S. Soluble Derivatives of Perylene and Naphthalene Diimide for n-Channel Organic Field-effect Transistors. *Org. Electron.* **2006**, *7*, 480−489.

(20) Jiang, W.; Xiao, C.; Hao, L.; Wang, Z.; Ceymann, H.; Lambert, C.; Di Motta, S.; Negri, F. Localization/Delocalization of Charges in Bay-Linked Perylene Bisimides. *Chem. - Eur. J.* **2012**, *18*, 6764−6775.

(21) Singh, R.; Giussani, E.; Mroz, M. M.; Fonzo, F. D.; Fazzi, D.; Cabanillas-González, J.; Oldridge, L.; Vaenas, N.; Kontos, A. G.; Falaras, P.; Grimsdale, A. C.; Jacob, J.; Müllen, K.; Keivanidis, P. E. On the Role of Aggregation Effects in the Performance of Perylene-Diimide based Solar Cells. *Org. Electron.* **2014**, *15*, 1347−1361.

(22) Chen, Z. J.; Stepanenko, V.; Dehm, V.; Prins, P.; Siebbeles, L. D. A.; Seibt, J.; Marquetand, P.; Engel, V.; Würthner, F. Photoluminescence and Conductivity of Self-assembled pi-pi Stacks of Perylene Bisimide Dyes. *Chem. - Eur. J.* **2007**, *13*, 436−449.

(23) Chellappan, K. V.; Kandappa, S. K.; Rajaram, S.; Narayan, K. S. Ferroelectric Polymer Matrix for Probing Molecular Organization in Perylene Diimides. *J. Phys. Chem. Lett.* **2015**, *6*, 224−229.

(24) Hartnett, P. E.; Timalsina, A.; Matte, H. S. S. R.; Zhou, N.; Guo, X.; Zhao, W.; Facchetti, A.; Chang, R. P. H.; Hersam, M. C.; Wasielewski, M. R.; Marks, T. J. Slip-Stacked Perylenediimides as an Alternative Strategy for High Efficiency Nonfullerene Acceptors in Organic Photovoltaics. *J. Am. Chem. Soc.* **2014**, *136*, 16345−16356.

(25) Shoaee, S.; Deledalle, F.; Tuladhar, P. S.; Shivanna, R.; Rajaram, S.; Narayan, K. S.; Durrant, J. R. A Comparison of Charge Separation Dynamics in Organic Blend Films Employing Fullerene and Perylene Diimide Electron Acceptors. *J. Phys. Chem. Lett.* **2015**, *6*, 201−205.

DOI: 10.1021/acsami.5b08224
ACS Appl. Mater. Interfaces 2015, 7, 24876−24886

(26) Gehrig, D. W.; Roland, S.; Howard, I. A.; Kamm, V.; Mangold, H.; Neher, D.; Laquai, F. d. r. Efficiency-Limiting Processes in Low-Bandgap Polymer:Perylene Diimide Photovoltaic Blends. *J. Phys. Chem. C* **2014**, *118*, 20077−20085.
(27) Shivanna, R.; Shoaee, S.; Dimitrov, S.; Kandappa, S. K.; Rajaram, S.; Durrant, J. R.; Narayan, K. S. Charge Generation and Transport in Efficient Organic Bulk Heterojunction Solar Cells with a Perylene Acceptor. *Energy Environ. Sci.* **2014**, *7*, 435−441.
(28) Ye, T.; Singh, R.; Butt, H.-J.; Floudas, G.; Keivanidis, P. E. Effect of Local and Global Structural Order on the Performance of Perylene Diimide Excimeric Solar Cells. *ACS Appl. Mater. Interfaces* **2013**, *5*, 11844−11857.
(29) Chen, Z.; Baumeister, U.; Tschierske, C.; Wüerthner, F. Effect of Core Twisting on Self-Assembly and Optical Properties of Perylene Bisimide Dyes in Solution and Columnar Liquid Crystalline Phases. *Chem. - Eur. J.* **2007**, *13*, 450−465.
(30) Howard, I. A.; Laquai, F.; Keivanidis, P. E.; Friend, R. H.; Greenham, N. C. Perylene Tetracarboxydiimide as an Electron Acceptor in Organic Solar Cells: A Study of Charge Generation and Recombination. *J. Phys. Chem. C* **2009**, *113*, 21225−21232.
(31) Lindquist, R. J.; Lefler, K. M.; Brown, K. E.; Dyar, S. M.; Margulies, E. A.; Young, R. M.; Wasielewski, M. R. Energy Flow Dynamics within Cofacial and Slip-Stacked Perylene-3,4-dicarboximide Dimer Models of π-Aggregates. *J. Am. Chem. Soc.* **2014**, *136*, 14912−14923.
(32) Fischer, D.; Naundorf, G.; Klöpffer, D. Light Absorption by Pyrene Single Crystals Between 4 and 300K: A Search for the Ground- to Excimer State Absorption. *Z. Naturforsch., A: Phys. Sci.* **1973**, DOI: 10.1515/zna-1973-0620.
(33) Singh, R.; Aluicio-Sarduy, E.; Kan, Z.; Ye, T.; MacKenzie, R. C. I.; Keivanidis, P. E. Fullerene-free Organic Solar Cells with an Efficiency of 3.7% Based on a Low-Cost Geometrically Planar Perylene Diimide Monomer. *J. Mater. Chem. A* **2014**, *2*, 14348−14353.
(34) Aluicio-Sarduy, E.; Singh, R.; Kan, Z.; Ye, T.; Baidak, A.; Calloni, A.; Berti, G.; Duò, L.; Iosifidis, A.; Beaupré, S.; Leclerc, M.; Butt, H.-J.; Floudas, G.; Keivanidis, P. E. Elucidating the Impact of Molecular Packing and Device Architecture on the Performance of Nanostructured Perylene Diimide Solar Cells. *ACS Appl. Mater. Interfaces* **2015**, *7*, 8687−8698.
(35) Dittmer, J. J.; Marseglia, E. A.; Friend, R. H. Electron Trapping in Dye/Polymer Blend Photovoltaic Cells. *Adv. Mater.* **2000**, *12*, 1270−1274.
(36) Di Donato, E.; Fornari, R. P.; Di Motta, S.; Li, Y.; Wang, Z.; Negri, F. n-Type Charge Transport and Mobility of Fluorinated Perylene Bisimide Semiconductors. *J. Phys. Chem. B* **2010**, *114*, 5327−5334.
(37) Mizoshita, N.; Tani, T.; Inagaki, S. Highly Conductive Organosilica Hybrid Films Prepared from a Liquid-Crystal Perylene Bisimide Precursor. *Adv. Funct. Mater.* **2011**, *21*, 3291−3296.
(38) Takada, T.; Ashida, A.; Nakamura, M.; Fujitsuka, M.; Majima, T.; Yamana, K. Photocurrent Generation Enhanced by Charge Delocalization over Stacked Perylenediimide Chromophores Assembled within DNA. *J. Am. Chem. Soc.* **2014**, *136*, 6814−6817.
(39) Rajaram, S.; Shivanna, R.; Kandappa, S. K.; Narayan, K. S. Nonplanar Perylene Diimides as Potential Alternatives to Fullerenes in Organic Solar Cells. *J. Phys. Chem. Lett.* **2012**, *3*, 2405−2408.
(40) Ie, Y.; Sakurai, T.; Jinnai, S.; Karakawa, M.; Okuda, K.; Mori, S.; Aso, Y. Three-Dimensional Electron-Accepting Compounds Containing Perylene bis(dicarboximide)s as n-Type Organic Photovoltaic Materials. *Chem. Commun.* **2013**, *49*, 8386−8388.
(41) Ramanan, C.; Kim, C. H.; Marks, T. J.; Wasielewski, M. R. Excitation Energy Transfer within Covalent Tetrahedral Perylenediimide Tetramers and Their Intermolecular Aggregates. *J. Phys. Chem. C* **2014**, *118*, 16941−16950.
(42) Chen, W.; Yang, X.; Long, G.; Wan, X.; Chen, Y.; Zhang, Q. A Perylene Diimide (PDI)-Based Small Molecule with Tetrahedral Configuration as a Non-Fullerene Acceptor for Organic Solar Cells. *J. Mater. Chem. C* **2015**, *3*, 4698−4705.
(43) Liu, Y.; Mu, C.; Jiang, K.; Zhao, J.; Li, Y.; Zhang, L.; Li, Z.; Lai, J. Y. L.; Hu, H.; Ma, T.; Hu, R.; Yu, D.; Huang, X.; Tang, B. Z.; Yan, H. A Tetraphenylethylene Core-Based 3D Structure Small Molecular Acceptor Enabling Efficient Non-Fullerene Organic Solar Cells. *Adv. Mater.* **2015**, *27*, 1015−1020.
(44) Liu, S.-Y.; Wu, C.-H.; Li, C.-Z.; Liu, S.-Q.; Wei, K.-H.; Chen, H.-Z.; Jen, A. K.-Y. A Tetraperylene Diimides Based 3D Nonfullerene Acceptor for Efficient Organic Photovoltaics. *Adv. Sci.* **2015**, DOI: 10.1002/advs.201500014.
(45) Chen, Y.; Zhang, X.; Zhan, C.; Yao, J. In-Depth Understanding of Photocurrent Enhancement in Solution-Processed Small-Molecule:-Perylene Diimide Non-Fullerene Organic Solar Cells. *Phys. Status Solidi A* **2015**, *212*, 1961.
(46) Zhao, J.; Li, Y.; Lin, H.; Liu, Y.; Jiang, K.; Mu, C.; Ma, T.; Lai, J. Y. L.; Yan, H.; et al. High-Efficiency Non-Fullerene Organic Solar Cells Enabled by a Difluorobenzothiadizole-Based Donor Polymer Combined with a Properly Matched Small Molecule Acceptor. *Energy Environ. Sci.* **2015**, *8*, 520−525.
(47) Wu, C.-H.; Chueh, C.-C.; Xi, Y.-Y.; Zhong, H.-L.; Gao, G.-P.; Wang, Z.-H.; Pozzo, L.-D.; Wen, T.-C.; Jen, A. K.-Y. Influence of Molecular Geometry of Perylene Diimide Dimers and Polymers on Bulk Heterojunction Morphology Toward High-Performance Non-fullerene Polymer Solar Cells. *Adv. Funct. Mater.* **2015**, *25*, 5326.
(48) Sun, D.; Meng, D.; Cai, Y.; Fan, B.; Li, Y.; Jiang, W.; Huo, L.; Sun, Y.; Wang, Z. Non-Fullerene-Acceptor-Based Bulk-Heterojunction Organic Solar Cells with Efficiency over 7%. *J. Am. Chem. Soc.* **2015**, *137*, 11156.
(49) Lu, Z.; Jiang, B.; Zhang, X.; Tang, A.; Chen, L.; Zhan, C.; Yao, J. Perylene−Diimide Based Non-Fullerene Solar Cells with 4.34% Efficiency through Engineering Surface Donor/Acceptor Compositions. *Chem. Mater.* **2014**, *26*, 2907−2914.
(50) Sharenko, A.; Gehrig, D.; Laquai, F.; Nguyen, T.-Q. The Effect of Solvent Additive on the Charge Generation and Photovoltaic Performance of a Solution-Processed Small Molecule:Perylene Diimide Bulk Heterojunction Solar Cell. *Chem. Mater.* **2014**, *26*, 4109−4118.
(51) Chen, Y.; Zhang, X.; Zhan, C.; Yao, J. Origin of Effects of Additive Solvent on Film-Morphology in Solution-Processed Non-fullerene Solar Cells. *ACS Appl. Mater. Interfaces* **2015**, *7*, 6462−6471.
(52) Zang, Y.; Li, C.-Z.; Chueh, C.-C.; Williams, S. T.; Jiang, W.; Wang, Z.-H.; Yu, J.-S.; Jen, A. K. Y. Integrated Molecular, Interfacial, and Device Engineering towards High-Performance Non-Fullerene Based Organic Solar Cells. *Adv. Mater.* **2014**, *26*, 5708−5714.
(53) Shivanna, R.; Rajaram, R.; Narayan, K. S. Interface Engineering for Efficient Fullerene-Free Organic Solar Cells. *Appl. Phys. Lett.* **2015**, *106*, 123301.
(54) Ye, L.; Sun, K.; Jiang, W.; Zhang, S.; Zhao, W.; Yao, H.; Wang, Z.; Hou, J. Enhanced Efficiency in Fullerene-Free Polymer Solar Cell by Incorporating Fine-designed Donor and Acceptor Materials. *ACS Appl. Mater. Interfaces* **2015**, *7*, 9274−9280.
(55) Förster, T. Transfer Mechanisms of Electronic Excitation. *Discuss. Faraday Soc.* **1959**, *27*, 7−17.
(56) Engmann, S.; Bokel, F. A.; Herzing, A. A.; Ro, H. W.; Girotto, C.; Caputo, B.; Hoven, C. V.; Schaible, E.; Hexemer, A.; DeLongchamp, D. M.; Richter, L. J. Real-Time X-Ray Scattering Studies of Film Evolution in High Performing Small-Molecule−Fullerene Organic Solar Cells. *J. Mater. Chem. A* **2015**, *3*, 8764−8771.
(57) Atkins, P.; de Paula, J. *Physical Chemistry*, 9th ed.; Macmillan Education: U.K., 2010.
(58) Chi, C.; Im, C.; Enkelmann, V.; Ziegler, A.; Lieser, G.; Wegner, G. Monodisperse Oligofluorenes with Keto Defect as Models to Investigate the Origin of Green Emission From Polyfluorenes: Syntheis, Self-Assembly, and Photophysical Properties. *Chem. - Eur. J.* **2005**, *11*, 6833−6845.
(59) Bednarz, M.; Malyshev, V. A.; Knoester, J. Low-Temperature Dynamics of Weakly Localized Frenkel Excitons in Disordered Linear Chains. *J. Chem. Phys.* **2004**, *120*, 3827−3840.
(60) Wiesenhofer, H.; Zojer, E.; List, E. J. W.; Scherf, U.; Bredas, J. L.; Beljonne, D. Molecular Origin of the Temperature-Dependent

DOI: 10.1021/acsami.5b08224
ACS Appl. Mater. Interfaces 2015, 7, 24876−24886

Energy Migration in a Rigid-Rod Ladder-Phenylene Molecular Host. *Adv. Mater.* **2006**, *18*, 310−314.
(61) Wantz, G.; Hirsch, L.; Huby, N.; Vignau, L.; Barriere, A. S.; Parneix, J. P. Temperature-Dependent Electroluminescence Spectra of Poly(phenylene-vinylene) Derivatives-Based Polymer Light-Emitting Diodes. *J. Appl. Phys.* **2005**, *97*, 034505.
(62) Guha, S.; Rice, J. D.; Yau, Y. T.; Martin, C. M.; Chandrasekhar, M.; Chandrasekhar, H. R.; Guentner, R.; de Freitas, P. S.; Scherf, U. Temperature-Dependent Photoluminescence of Organic Semiconductors with Varying Backbone Conformation. *Phys. Rev. B: Condens. Matter Mater. Phys.* **2003**, *67*, 125204.
(63) Alamiry, M. A. H.; Harriman, A.; Mallon, L. J.; Ulrich, G.; Ziessel, R. Energy- and Charge-Transfer Processes in a Perylene-BODIPY-Pyridine Tripartite Array. *Eur. J. Org. Chem.* **2008**, *16*, 2774−2782.
(64) Curutchet, C.; Mennucci, B.; Scholes, G. D.; Beljonne, D. oes Forster Theory Predict the Rate of Electronic Energy Transfer for a Model Dyad at Low Temperature? *J. Phys. Chem. B* **2008**, *112*, 3759−3766.
(65) Rothberg, L. J.; Yan, M.; Papadimitrakopoulos, F.; Galvin, M. E.; Kwock, E. W.; Miller, T. M. Photophysics of Phenylenevinylene Polymers. *Synth. Met.* **1996**, *80*, 41−58.
(66) Foster, S.; Finlayson, C. E.; Keivanidis, P. E.; Huang, Y.-S.; Hwang, I.; Friend, R. H.; Otten, M. B. J.; Lu, L.-P.; Schwartz, E.; Nolte, R. J. M.; Rowan, A. E. Improved Performance of Perylene-Based Photovoltaic Cells Using Polyisocyanopeptide Arrays. *Macromolecules* **2009**, *42*, 2023−2030.

DOI: 10.1021/acsami.5b08224
ACS Appl. Mater. Interfaces 2015, 7, 24876−24886